Journal of Fluids and Structures (2002) **16**(3), 391–416
doi:10.1006/jfls.2001.0425, available online at http://www.idealibrary.com on IDEAL®

NONLINEAR INERTIAL LOADING. PART I: ACCELERATIONS IN STEEP 2-D WATER WAVES

C. SWAN AND T. BASHIR

Department of Civil & Environmental Engineering, Imperial College of Science Technology & Medicine, London SW7 2BU, UK

AND

O. T. GUDMESTAD

Statoil, 4035 Stavanger, Norway and Stavanger College, Stavanger, Norway

(Received 13 October 2000, and in final form 3 July 2001)

This paper reports on a new series of laboratory observations in which both the unsteady and the convective components of the water particle acceleration arising beneath an extreme two-dimensional transient wave were determined. The waveform investigated was produced by focusing frequency components within an irregular wave train, such that a large number of zero up-crossings arise at one point in space and time. For a given underlying set of frequency components, this produces an extreme event that has the maximum wave slope and therefore also the largest horizontal water particle accelerations. Spectral analysis, based upon the water surface elevation measured at the focal location, confirms that there are significant transfers of energy into the high-frequency components. Neither a linear random wave theory nor a steady nonlinear wave theory, both of which are commonly used in design applications, are able to correctly model these frequency components. As a result, such solutions provide a poor description of the large unsteady accelerations arising close to the water surface. Furthermore, since they are also unable to model the spatial evolution of the wave group, inaccurate predictions of the convective accelerations result. In contrast, a fully nonlinear unsteady wave theory, similar to that originally proposed by Fenton & Rienecker (1980), provides a good description of the laboratory data. To assess the importance of the nonlinear accelerations the inertia forces acting on a vertical, surface-piercing, cylinder are calculated and comparisons made with the nonlinear slender body forces identified by Rainey (1989, 1995). These comparisons confirm the importance of the applied wave model and suggest that the dominant contribution to the high-frequency forcing arises due to the nonlinearity of the wave motion. These results have applications in Offshore Engineering where transient structural deflections, occurring at frequencies well above the wave frequency, have been observed in a number of deep-water structures.

1. INTRODUCTION

ALTHOUGH THE DESCRIPTION OF EXTREME OCEAN WAVES has been the subject of sustained interest in recent years, the majority of this work has sought to define the characteristics of the largest or highest waves in which the maximum water particle velocities arise. This emphasis is related to the fact that in Offshore Engineering such waves define the design conditions for many classes of fixed and floating structures. For example, if one considers a typical steel space frame, or lattice structure, the diameter of the individual members (D) will be such that the Keulegan–Carpenter number $\mathrm{KC} = UT/D$, where U is the maximum wave-induced orbital velocity and T is the wave period, is greater than 20. In this case, the

0889–9746/02/030391 + 26 $35.00/0

viscous drag forces dominate and the applied forces are proportional to the square of the incident water particle velocities measured (or predicted) in the absence of the structure. Alternatively, if the diameter of an individual member increases such that $KC \leq 5$, the potential flow forces will exceed the viscous drag forces. If, in this case, it is again assumed that the structure causes no disturbance to the incident wavefield (i.e., there is no scattering or diffraction) the maximum force per unit length is dependent upon the water particle accelerations rather than the velocities. As a result, a second category of extreme waves is required in which the slope of the water surface, rather than the crest elevation, is maximised. It is these waves that the present paper will address.

2. BACKGROUND

Recent work concerning the description of extreme waves in random or irregular seas has clearly demonstrated that in the vicinity of an extreme wave crest both the water surface elevation and the underlying water particle velocities differ significantly from the linear sum of the component free waves. For example, Baldock *et al.* (1996), hereafter referred to as BST, provide a detailed laboratory study of large transient water waves. In each of their examples, a large focused wave group was created by simultaneously generating a large number of frequency components, and adjusting their relative phasing so that constructive interference between the wave crests occurred at one point in space and time. This approach has been adopted by several previous researchers, notably Longuet-Higgins (1974) and Rapp & Melville (1990), and is believed to be representative of the way in which large deep-water ocean waves evolve in a broad-banded sea. Evidence to support this view is provided by a recent analysis of field data gathered in the northern North Sea (Jonathan & Taylor 1995).

BST investigated the nonlinearity of these large wave events by contrasting the time history of the water surface elevation, $\eta(t)$, recorded at the focal point with a linear solution based on the sum of the free waves generated at the wave paddle. Comparisons of this type confirm that these waves are indeed highly nonlinear, with maximum crest elevations as much as 30% larger than that predicted by linear theory. Indeed, the general form of these focused wave groups is such that the central wave crest is both higher and narrower, while the adjacent wave troughs are broader and less deep. Results of this type, together with detailed spectral analysis of the measured water surface elevations, led BST to suggest that during the evolution of a focused wave event the local wave–wave interactions produce a significant shift of energy into the high-frequency components. Indeed, further comparisons with a second-order theory based on the sum of the wave–wave interactions first identified by Longuet-Higgins & Stewart (1960) confirmed that these interactions occur at a higher order of wave steepness ($\mathcal{O}(a^3k^3)$ and above, where a is the wave amplitude and k is the wavenumber). These results are consistent with the numerical calculations presented by Longuet-Higgins (1987), and suggest that an adequate representation of an extreme wave crest can only be achieved if both the nonlinearity and the unsteadiness are incorporated within the wave model.

Alongside the developments noted above, other researchers have sought to quantify the nonlinear contributions to the potential flow loading. Much of this work was motivated by Lighthill (1979) in which he stated that there were additional nonlinear potential flow loads which should be added to the standard Morison's inertia term. More recently, Rainey (1989, 1995*a*, *b*), Manners & Rainey (1992), Faltinsen *et al.* (1995) and Newman (1996) have also tackled this problem. Detailed discussions of these papers will be left until Section 6. However, it is important to note that there now appears to be considerable agreement regarding the description of the nonlinear forces, although there is perhaps ongoing debate

as to the wave conditions within which the solutions are valid. In particular, an additional second-order force (often referred to as the axial divergence term) has been derived independently by Rainey (1989) and Faltinsen *et al.* (1995). Furthermore, although the third-order loads predicted by Manners & Rainey (1992) appear substantially smaller than those derived by Faltinsen *et al.* (1995), the latter solution includes the local disturbance of the wavefield due to the presence of the cylinder, whereas the former was derived for a genuinely slender body in that the position of the water surface was unaffected by the structure. After correcting for this effect, Rainey (1995*a*) provides a unified result.

Although the individual contributions noted above are undoubtedly significant, it is important to note that recent papers have developed along two quite separate strands: those primarily concerned with the nonlinearity of extreme ocean waves, and those seeking to identify the additional nonlinear forces appropriate to a potential flow model. The present paper will attempt to bridge this gap, and will demonstrate that an accurate description of the nonlinear water particle accelerations is critical to the prediction of the applied fluid loading.

These results have important practical implications in that it is now widely recognised that large offshore platforms may be susceptible to transient structural deflections occurring at natural frequencies that are substantially higher than the dominant wave frequencies. These events, which are commonly referred to as "ringing", have been observed in both model test data (Stansberg 1997) and field data from instrumented platforms. However, despite a concerted research effort, it is not yet possible to accurately predict either the occurrence or the magnitude of this dynamic response.

The present paper continues in Section 3 with a brief description of a kinematics model that is capable of incorporating both the nonlinearity and the unsteadiness of an extreme wave group. In Section 4, a new experimental study is described in which an irregular wave train is generated, with the phasing of the individual wave components adjusted so that the focused or extreme event involves maximising the wave slope rather than the crest elevation. Kinematics data is gathered at a large number of spatial positions so that both the unsteady and the convective components of acceleration can be defined throughout the flow field. Comparisons between the wave model and the measured data are presented in Section 5. Further comparisons with typical design solutions, involving a nonlinear steady wave theory and a linear random wave theory, highlight the importance of neglecting either the unsteadiness or the nonlinearity of an extreme wave event. Having validated the wave model, the magnitude of the inertial loads acting on a vertical, surface-piercing, cylinder are assessed in Section 6. The paper concludes in Section 7 with a number of recommendations concerning the description of an extreme wave event and the calculation of the associated inertial loads.

3. WAVE MODELLING

We have already noted that the experimental data presented by BST suggest that a successful wave model must include both the nonlinearity and the unsteadiness of an extreme wave event. Unfortunately, the commonly applied wave theories tend to neglect one or other of these characteristics. For example, both a fifth-order Stokes solution (Fenton 1985) or a higher-order stream function solution (Dean 1965) assumes that the wave-form propagates without change of form; while a linear random wave theory neglects the nonlinearity and assumes that all the wave components are freely propagating and therefore satisfy the linear dispersion equation. The only analytical model that partially includes both nonlinearity and unsteadiness is the second-order solution originally proposed by Longuet-Higgins & Stewart (1960) and further developed by Sharma & Dean (1981). However,

Longuet-Higgins (1987) has already demonstrated that for the simplified case of short waves propagating on long waves, the nonlinear wave–wave interactions will be significantly larger than those predicted by the second-order solution as the steepness of the long wave increases. More recently, BST demonstrated experimentally that this is also true in steep broad-banded sea states. These arguments concerning the extent of the nonlinearity are equally applicable to the hybrid second-order models (Stansberg 1993; Ye & Zhang 1994; Zhang *et al.* 1998) in which various forms of filtering are applied in an attempt to identify the free waves from a measured ocean spectrum.

In addition to the wave models discussed above, there are two categories of wave solutions that attempt to include both nonlinearity and unsteadiness. The first may be described as approximate, being based upon a time history of the water surface elevation recorded at one spatial location, while the second involves the "exact" numerical solution of the nonlinear free surface boundary conditions.

3.1. Approximate Numerical Models

This category of solution includes both the local Fourier series solution (Sobey 1992) and the double Fourier series solution (Baldock & Swan 1994). A full review of these methods is given by Smith & Swan (1997). In the context of the present study, it is merely sufficient to note that the largest errors associated with the local Fourier series solution arise where the surface elevation exhibits little or no curvature. Unfortunately, this corresponds to the point of inflection where the horizontal water particle accelerations are a maximum. Furthermore, since the local Fourier series solution is based upon a fit to the surface elevation in a small (localised) window, it is unable to resolve the frequency-difference terms corresponding to the set-down beneath the wave group. As a result, the solution tends to overestimate the horizontal velocities, and hence also the accelerations, with increasing distance beneath the water surface. In contrast, the double Fourier series solution is restricted, for computational reasons, in terms of the number of harmonics that can conveniently be included within the solution matrix. As a result, Smith & Swan (1997) conclude that the truncation of the double Fourier series solution will lead to an underestimate of the maximum near-surface velocities, and hence also the corresponding water particle accelerations, in steep near-breaking waves.

3.2. "Exact" Numerical Calculations

If the velocity potential, ϕ, is defined so that the horizontal and vertical velocity components are given by $u = \phi_x$ and $w = \phi_z$ respectively, the boundary conditions acting on the free surface, $z = \eta(x, t)$, are given by

$$\eta_t = \phi_z - \eta_x \phi_x, \qquad \phi_t = -(g\eta + \tfrac{1}{2}[\phi_x^2 + \phi_y^2]) \tag{1}$$

where t indicates time, g is the gravitational acceleration and (x, z) are the usual Cartesian co-ordinates in which x is measured in the direction of wave propagation and z vertically upwards from the still water level. Longuet-Higgins & Cokelet (1976) first noted that in this form there are no time derivatives on the right-hand side of either equation. As a result, if a spatial description of both the water surface elevation, $\eta(x)$, and the velocity potential, $\phi(\eta, x)$, are known at some initial time, $t = t_0$, the solution can be time stepped to achieve a spatial description of the wavefield at $t = t_0 + \Delta t$, where Δt corresponds to a small time increment. This process is then repeated for a large number of time steps, so that the evolution of a wavefield can be modelled over large times. In the present study, numerical calculations were undertaken using a time-stepping procedure similar to that outlined by

Fenton & Rienecker (1980). This approach is based upon a Fourier representation of the surface profile

$$\eta = a_0 + \sum_{n=1}^{N-1} \{a_n \cos(nk_0 x) + b_n \sin(nk_0 x)\} + a_N \cos(Nk_0 x) \tag{2}$$

with the corresponding velocity potential defined by

$$\phi = A_0 + \sum_{n=1}^{N-1} \left\{ (A_n \cos(nk_0 x) + B_n \sin(nk_0 x)) \frac{\cosh(nk_0(z+d))}{\sinh(nk_0 d)} \right\}$$
$$+ A_N \cos(Nk_0 x) \frac{\cosh(Nk_0(z+d))}{\sinh(Nk_0 d)}, \tag{3}$$

where d is the constant water depth, the unknown coefficients (a_n, b_n, A_n, B_n) are assumed to be functions of time only, and k_0 is the fundamental wavenumber or $2\pi/\lambda_0$, where λ_0 is the fundamental wavelength or the length scale over which the solution is assumed periodic.

In this form the velocity potential ϕ, equation (3), exactly satisfies both the governing field equation ($\nabla^2\phi = 0$) and the bottom boundary condition [$\phi_z = 0$ on $(z = -d)$]. As a result, the required solution merely involves the determination of the unknown coefficients at each time step. If initial values (corresponding to $t = t_0$) of both the water surface elevation, $\eta(x)$, and the velocity potential, $\phi(x, z)$, are specified at a total of $2N$ locations, which are equally spaced over the fundamental wavelength, a total of $4N$ linear simultaneous equations are produced by applying the nonlinear free surface boundary conditions [equations (1)] at each spatial location. These are sufficient to define the time derivatives of the unknown coefficients. To simplify this procedure the surface elevation [equation (2)], and hence its time derivative, is expressed in terms of a standard Fourier series so that $\mathrm{d}a/\mathrm{d}t$ and $\mathrm{d}b/\mathrm{d}t$ can be solved rapidly using a fast Fourier transform. Unfortunately, the depth-variation included within the velocity potential [equation (3)] precludes this approach and consequently $\mathrm{d}A/\mathrm{d}t$ and $\mathrm{d}B/\mathrm{d}t$ must be solved by lower–upper (LU) matrix decomposition. This latter task accounts for the majority of the computational effort.

Having defined the time derivatives of the coefficients, a standard time-stepping procedure is used to achieve a new solution for η and ϕ at $t = t_0 + \Delta t$. After comparing several different time-stepping procedures the Adams–Bashford–Moulton predictor–corrector method, similar to that employed by Longuet-Higgins & Cokelet (1976), was shown to provide the best combination of accuracy, stability and efficiency. Gear (1971) outlines this method such that any function $f(t + \Delta t)$ is given by

$$f(t+\Delta t) = f(t) + \frac{\Delta t}{24}(9f_t^{\bullet}(t+\Delta t) + 19f_t(t) - 5f_t(t-\Delta t) + f_t(t-2\Delta t))$$

with (4)

$$f^*(t+\Delta t) = f(t) + \frac{\Delta t}{24}(55f_t(t) - 59f_t(t-\Delta t) + 37f_t(t-2\Delta t) - 9f_t(t-3\Delta t)),$$

where the scheme has a truncation error of order (Δt^5). The only disadvantage of this approach is that it requires information from more than one previous time step. To overcome this difficulty, the first three time steps were undertaken using a fourth-order Runge–Kutta scheme.

To ensure that the calculations outlined above maintained an appropriate level of accuracy, and that no spurious numerical instabilities arose, two precautions were found necessary. Firstly, a relatively small time-step was adopted. If $f_{\max}$ is the maximum

anticipated frequency at which there is any appreciable energy, $\Delta t = 0{\cdot}04/f_{\max}$ was found to be appropriate for all cases. Secondly, to prevent the growth of any numerical instabilities (which typically arise in the highest wavenumber components) the largest wavenumber, Nk_0, was limited to approximately 20 times the wavenumber corresponding to the peak of the input spectra. In this way, highly nonlinear, near-breaking, waves could be modelled without the need for additional numerical smoothing. In addition to these precautions, the scheme was continuously monitored during successive calculations. In particular, to ensure that the scheme was not adversely affected by truncation errors, the amplitudes of the largest wavenumber components (a_N, A_N) should remain negligible at all times. If this is not the case Nk_0 must be increased, although its upper limit is defined by the stability requirement noted above. Furthermore, it is clear that the total wave energy within the spatial domain must be conserved (Zakharov 1968). To ensure that this was indeed the case, the total wave energy was calculated at every time step. Comparisons both between successive time steps, and after a large number of time steps, confirm that in all cases the total energy was conserved to within 0·04%.

It should be noted that although the scheme outlined above provides a relatively simple method of defining the nonlinear characteristics of transient water waves, it is in no sense unique. Alternative time-stepping solutions proposed by Longuet-Higgins & Cokelet (1976), Dold & Peregrine (1984) and, more recently, Craig & Sulem (1993) are equally applicable. Indeed, given the nature of the matrix decomposition noted above, these alternative methods are computationally more efficient. However, the present paper does not set out to recommend one time-stepping scheme over another, but rather to demonstrate that an accurate prediction of the water particle kinematics requires a wave model which is both fully nonlinear and dispersive, and that this has important implications for the prediction of the nonlinear potential wave loading.

4. EXPERIMENTAL WORK

4.1. Apparatus

The experimental investigation was undertaken within a large wave channel located in the Department of Civil & Environmental Engineering at Imperial College (Figure 1). This facility is 65 m long, 2·8 m wide, and is equipped with a numerically controlled wave paddle, capable of working in a range of water depths ($0{\cdot}5\,\text{m} \leq d \leq 1{\cdot}2\,\text{m}$). In the present investigation the water depth was maintained at $d = 0{\cdot}9$ m, such that the extreme waves were located in deep water ($k_p d \approx 3{\cdot}6$, where k_p is the wavenumber corresponding to the spectral peak). At the downstream end of the wave channel, the wave energy was dissipated on a 1:20 sloping beach. Preliminary measurements, covering an appropriate range of regular waves, indicated that the maximum reflection coefficient was of the order of 8%. Given the nature of the present study and, in particular, the need to consistently reproduce the desired waves at the test section, this level of uncertainty was considered unacceptable. Despite several modifications to the downstream conditions, including the installation of poly-ether foam to provide additional passive absorption (see BST), the reflection coefficient could not be significantly reduced. To overcome this problem, the measuring procedure (outlined below) was arranged so that the required waves were generated and sampled at the measuring section prior to the arrival of any unwanted reflections from the downstream end of the wave flume.

Within the present study, the water surface elevation was measured using an array of surface-piercing wave gauges. Each gauge consists of two vertical wires, each 1 mm in diameter spaced 10 mm apart, and provides a time history of the water surface elevation,

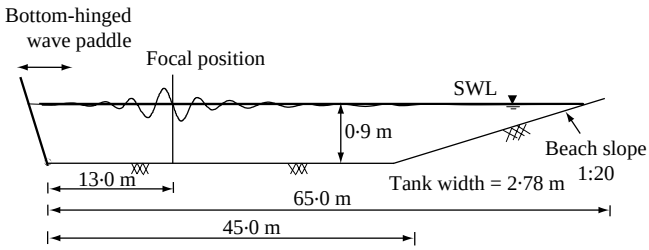

Figure 1. Experimental apparatus.

$\eta(t)$, at a fixed spatial location. Previous measurements described by BST have shown that these gauges produce no significant disturbance of the flow field, and have an accuracy of $\pm 0{\cdot}5$ mm. In addition to the surface elevation records, the underlying water particle velocities were measured using a laser Doppler anemometer (LDA). The system employed was based upon a 35 mW helium–neon laser, and was used to create a two-beam arrangement from which one component of the water particle velocity could be measured. Given the layout of the wave flume, particularly the restricted optical access, the laser beams were passed down a fibre optic cable terminating at the so-called "fibre-head". This component of the apparatus is cylindrical with an outside diameter of 12 mm and an overall length of 125 mm. At its downstream end, the laser beams emerge through a 50 mm focal length converging lens to produce an intersection or measuring volume estimated to be $0{\cdot}5\,\text{mm}^3$. The arrangement was based on a "back-scattered" configuration so that the receiving camera (or photo-multiplier) used to record the Doppler bursts was built into the fibre-head. As a result, this was the only component of the LDA close to the measuring volume. Previous work (Johannessen and Swan 2001) has shown that provided the fibre-head is positioned perpendicular to the plane of the wave motion, this method of measurement produces no significant disturbance of the flow field at the measuring point. To manipulate the position of the measuring point the fibre-head was supported in a vertical traverse, which was itself attached to a movable carriage mounted on rails located along the top of the wave flume. Using this arrangement, the measuring point could be located anywhere along the centreline of the wave flume with a positional accuracy of ± 1 mm in the horizontal and $\pm 0{\cdot}5$ mm in the vertical.

To enhance the quality of the velocity data, trimon-supersilk (1000) was added locally, in small concentrations, to provide an effective seeding material. In the context of the present study, this addition is particularly important since the largest water particle accelerations occur within the crest–trough region where the velocity signals are intermittent. To ensure that the required velocity data is gathered close to the instantaneous water surface, the response time of the LDA must be reduced to an absolute minimum. Preliminary measurements suggest that this response is critically dependent upon the density of the seeding material. After repeated tests the best results were achieved when the seeding was diluted in slightly warm water ($\Delta\theta \approx 5^{\circ}$C) and discharged continuously through an array of hypodermic needles located approximately 0·5 m upstream. Using this approach, sufficient seeding was introduced close to the water surface and the time response of the LDA found to be of the order of 2–3 ms. As a result, the water particle kinematics could be consistently measured to within 5 mm of the water surface with an accuracy of $\pm 2\%$.

4.2. Wave Generation

To investigate both the unsteady and the convective components of acceleration beneath an extreme 2-D wave group, the time histories of both the horizontal and the vertical velocity

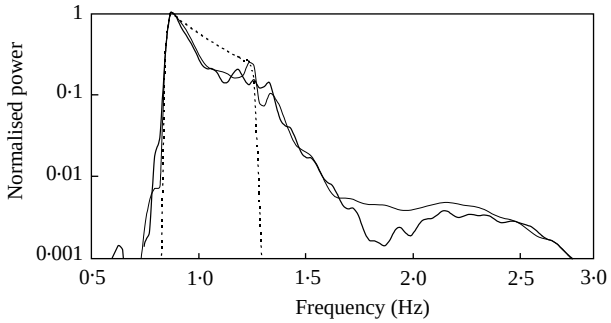

Figure 2. Power spectra based on $\eta(t)$ measured at the focus position: - - - - - -, input signal; ——, focused crests; ————, focused slopes.

components need to be measured at a large number of spatial locations. Given the inherent difficulty in obtaining this information with sufficient detail to define the acceleration components (particularly the convective terms), the present study considered one highly nonlinear wave group. BST demonstrated that for 2-D wave groups the importance of the nonlinear wave–wave interactions increases with the wave height, and reduces with increasing bandwidth. Accordingly, the wave group chosen in the present study was based upon a relatively narrow-banded spectrum consisting of 50 wave components that were equally spaced in the period range $0{\cdot}8 \leq T \leq 1{\cdot}2$ s and were of equal amplitude (α_n = constant, where α_n is the amplitude of the nth wave component). If A corresponds to the linear sum of the components wave amplitudes, $\alpha_n = A/50$, then the corresponding power spectrum, based upon the input signal sent to the wave paddle, decays according to ω^{-4}. At this point, it is perhaps important to note that the power spectrum associated with a wave group arising due to the focusing of discrete wave components is different from that associated with a continuous distribution of wave components each having a random phase. In the present tests, the power spectrum defining the input conditions, based on the freely propagating wave components generated at the wave paddle, is indicated by the dashed line in Figure 2.

Given the underlying wave spectrum, a linear analysis suggests that an extreme wave group (measured in terms of the water surface elevation) arises due to the summation (or focusing) of the component wave crests at one point in space and time; while an alternative extreme (measured in terms of the wave slope) arises due to the summation of the zero up-crossing points. The first of these cases has been addressed by BST and, more recently, by Johannessen & Swan (1997). In contrast, the second case has not previously been the subject of a laboratory investigation and is perhaps more applicable to the generation of the maximum water particle accelerations. However, it should be stressed that these arguments are based upon a simple linear interpretation, and that previous laboratory work has already confirmed the importance of the nonlinear wave–wave interactions. Indeed, BST suggest that in the case of a narrow-banded spectrum, the maximum water surface elevation may be as much as 30% larger than that predicted by linear theory ($\eta_{\max} = 1{\cdot}3\,A$). As a result, the associated wave slopes may in fact be steeper than those produced by the summation of zero up-crossings.

To resolve this issue the experimental programme first sought to identify which of these alternative wave groups was most appropriate. In both cases an input amplitude of $A = 50$ mm (or $\alpha_n = 1$ mm) was adopted, and the wave components (Figure 2) were generated at the paddle with their relative phasing adjusted such that according to linear theory the required focusing event occurred 13 m downstream of the paddle position. In practice,

TABLE 1
Extreme waves

Focused event	Linear amplitude sum, A (mm).	$\partial\eta/\partial t$(m/s)	$\partial\eta/\partial x$
Crests	48	0·46	−0·27
Slopes	48	0·55	−0·42

the actual focus point is shifted further downstream due to the nonlinear wave–wave interactions. However, BST have shown that the extent of this nonlinear shift is solely dependent upon the underlying frequency spectrum, and is therefore independent of whether the group is formed by focused crests, troughs or slopes. In consequence, the surface elevation records presented in Figure 3 were both measured 14·09 m downstream of the paddle. In this figure the open symbols correspond to the summation of wave crests, while the solid symbols correspond to the summation of wave slopes or zero up-crossings. In both these cases, as well as all subsequent cases, the time base has been shifted so that the focal event occurs at $t = 0$, with negative time ($t < 0$) occurring prior to the focal event, and positive time ($t > 0$) after. Spectral analysis of these data traces (Figure 2) suggest that the former case (corresponding to the summation of wave crests) involves a greater proportional shift of wave energy into the high frequencies and is therefore perhaps more nonlinear. However, detailed considerations of the water surface gradients relating to a slightly smaller wave ($A = 48$ mm) are presented in Table 1. These results confirm that the latter case (corresponding to the summation of wave slopes) involves the steepest wave profile in both space and time, and hence the maximum water particle accelerations. It is thus this type of focused event that will form the basis of the present investigation.

4.3. MEASURING PROCEDURE

Having chosen both the underlying wave spectra and the nature of the focusing event, the next step involved the generation of the desired wave at the measuring section, 13 m downstream of the wave paddle. Unfortunately, initial measurements confirmed that it was extremely difficult to adjust the relative phasing of the wave components, and then determine, with any degree of certainty, the exact spatial location at which the maximum wave slope arises. However, this difficulty does not arise in the case of a focused wave crest since the symmetry of the adjacent wave troughs (Figure 3) ensures that this event is easily identified. As a result, the following two-part procedure was adopted. Firstly, the relative phasing of the wave components was adjusted, using an iterative approach, until a focused wave crest was generated at the centre of the measuring section. A detailed description of this process is given in BST. Having achieved this, the second stage invoked the arguments (noted above) concerning the downstream shifting of the focal point, and merely involved adjusting the phase of each wave component by $\pi/2$. In this way, the focused event remains at the desired position, but corresponds to the summation of wave slopes and therefore represents the steepest wave profile.

Having produced the desired waveform at the measuring section, the nature of the velocity measurements (see above) required this wave profile to be consistently reproduced over a large number of individual runs with little or no variation in either space or time. Preliminary measurements confirmed that provided sufficient time was allowed for the wave flume to settle after each test run, repeated generations of the same wave group were

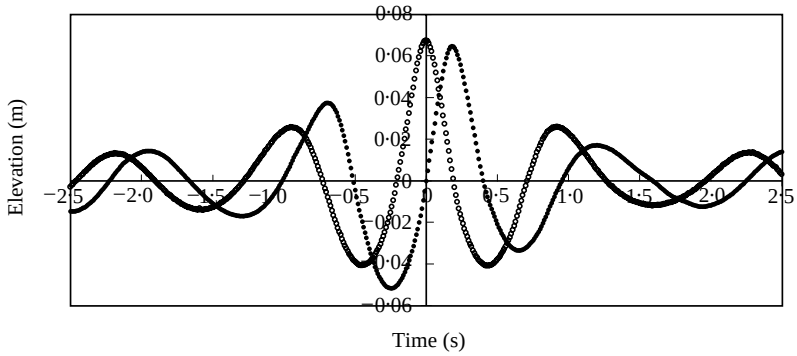

Figure 3. Water surface elevations, $\eta(t)$: ○, focused crests; ●, focused slopes.

TABLE 2
Spatial distribution of measuring positions (all dimensions in metres)

	$-0{\cdot}4 \le x \le -0{\cdot}2$ m	$-0{\cdot}2 \le x \le 0{\cdot}2$ m	$0{\cdot}2 \le x \le 0{\cdot}4$ m
$\eta(t) \ge z \ge -0{\cdot}05$ m	$\Delta x = 0{\cdot}050$ $\Delta z = 0{\cdot}0025$	$\Delta x = 0{\cdot}025$ $\Delta z = 0{\cdot}0025$	$\Delta x = 0{\cdot}050$ $\Delta z = 0{\cdot}0025$
$-0{\cdot}05 \ge z \ge -0{\cdot}20$ m	$\Delta x = 0{\cdot}050$ $\Delta z = 0{\cdot}010$	$\Delta x = 0{\cdot}025$ $\Delta z = 0{\cdot}010$	$\Delta x = 0{\cdot}050$ $\Delta z = 0{\cdot}010$
$-0{\cdot}20 \ge z \ge -0{\cdot}40$ m	$\Delta x = 0{\cdot}050$ $\Delta z = 0{\cdot}050$	$\Delta x = 0{\cdot}025$ $\Delta z = 0{\cdot}050$	$\Delta x = 0{\cdot}050$ $\Delta z = 0{\cdot}050$
$-0{\cdot}40 \ge z \ge -0{\cdot}90$ m	$\Delta x = 0{\cdot}050$ $\Delta z = 0{\cdot}100$	$\Delta x = 0{\cdot}025$ $\Delta z = 0{\cdot}100$	$\Delta x = 0{\cdot}050$ $\Delta z = 0{\cdot}100$

essentially identical. Indeed, the maximum variation at any spatial location was found to be less than 1% of the maximum wave height. This is close to the measuring accuracy of the wave gauges. As a result, velocity data gathered at different spatial locations during repeated generations were assembled to provide a full-field, time history of the water particle kinematics within the vicinity of the extreme wave event. Within the present tests, a total of 2500 runs were undertaken in which both the horizontal and the vertical velocity components were measured at 25 vertical sections within the region $-0{\cdot}4\,\text{m} \le x \le 0{\cdot}4\,\text{m}$, where $x = 0$ corresponds to the focal position. At each of these test-sections, the depth variation in the velocity components was recorded at some 50 spatial locations. The separation of these measuring points in both x and z was nonuniform, with more information recorded close to ($x = 0$, $z = 0$) where the largest water particle accelerations occur. The precise layout of the measuring points is indicated in Table 2.

At each of the 1250 spatial locations noted above, the velocity data (both u and w) were recorded for a total of 20 s at 100 Hz. To accompany each velocity record, two simultaneous measurements of the water surface elevation were also recorded (again at 100 Hz for 20 s). The first of these traces defines the surface profile directly above the intersection of the laser beams (i.e., the velocity measuring point), while the second describes the surface profile at the focus location ($x = 0$). This latter record acts both as a reference trace and ensures the consistency of the waveform. On the basis of this data we were able to define the temporal (t) and the spatial (x, z) variation in both the water particle kinematics, $u(x, z, t)$ and $w(x, z, t)$,

and the water surface elevation, $\eta(x, t)$. It is this information that will be used to define the acceleration "data" presented in Section 5.

5. DISCUSSION OF RESULTS

In order to model the experimental data, the numerical scheme outlined in Section 3 requires input in the form of a spatial description of both the water surface elevation, $\eta(x)$, and the velocity potential, $\phi(x)$, at some initial time ($t = t_0$). In the present example, this input is simply based upon the wave components generated at the wave paddle, and the nature of the focusing event. If all the generated waves are assumed to be linear and freely propagating, the surface profile at the instant of wave focusing can be predicted using linear theory ($\eta_L(x)$ at $t = 0$). This surface can, in turn, be represented by

$$\eta = \sum_{n=1}^{N-1} \{\alpha_n \cos(\omega_n t + \varepsilon_n)\cos(nk_0 x) + \alpha_n \sin(\omega_n t + \varepsilon_n)\sin(nk_0 x)\}, \tag{5}$$

where nk_0 defines the wavenumber of the nth component, ω_n the corresponding wave frequency derived from the linear dispersion relation, and ε_n a phase shift to allow the focusing of any part of the wave cycle ($\varepsilon_n = \pi/2$ to ensure the focusing of wave slopes). The amplitudes, α_n, of the individual wave components are determined by a least-squares minimisation in which equation (5) is matched to the linearly predicted water surface profile at the instant of wave focusing ($\eta_L(x)$ at $t = 0$). The principal advantage of this least-squares fit is that it allows the position of the wave components within the wavenumber spectrum to be finely controlled. This, in turn, allows a good fit to the linearly predicted surface elevation in the vicinity of a focussed event with relatively few wavenumber components. It is important to note that, when defining the initial conditions, many of the α_n values, particularly in the high wavenumber regime, must remain zero.

To achieve a good description of the evolving wave field using the Fourier representation outlined in Section 3, the fundamental wavenumber (k_0) must be small. This ensures that there are an adequate number of wave components within the initial input range. Furthermore, Nk_0 must be large so that no significant energy is present beyond the truncation of the series solution. This is particularly important as the nonlinear wave focuses and energy is transferred to the higher wavenumber, or wave frequency, components (see BST). Having defined appropriate values of N and k_0, an initial time $t = t_0$ (where $t_0 < 0$, since focusing occurs at $t = 0$) is chosen such that according to linear dispersion, both η and $\partial\eta/\partial x$ at $t = t_0$ are small everywhere over the fundamental wavelength, λ_0. Repeated calculations suggest that in the present case, a sufficient criterion is that the second-order correction (Longuet-Higgins & Stewart 1960) to any crest elevation within the fundamental domain should be less than 2% of the linearly predicted crest height. Having identified a suitable t_0, the initial coefficients appropriate to the commencement of the time-stepping procedure [equations (2) and (3)] are given by

$$\begin{aligned} &a_0 = a_N = A_0 = A_N = 0, \\ &a_n = \alpha_n \cos(\omega_n t_0 + \varepsilon_n), \quad b_n = \alpha_n \sin(\omega_n t_0 + \varepsilon_n), \\ &A_n = -\frac{\alpha_n \omega_n}{nk_0} \sin(\omega_n t_0 + \varepsilon_n), \quad B_n = -\frac{\alpha_n \omega_n}{nk_0} \cos(\omega_n t_0 + \varepsilon_n). \end{aligned} \tag{6}$$

By defining the initial conditions in this way we ensure that the linear characteristics of the focused wave group are accurately reproduced in the vicinity of the focal event ($x = t = 0$). This is, of course, an essential prerequisite when attempting to model the

nonlinear properties of any large wave event. Furthermore, the present method has the added advantage that it does not involve successive iteration, nor does it require a prior description of the nonlinear water surface profile. As such, it is in marked contrast to the results presented by Skyner (1996) and is appropriate to design calculations. The data presented within this section is divided into two parts. The first concerns the time history of the velocity components measured at specific spatial locations, and is used to define the unsteady acceleration components ($\partial u/\partial t$, and $\partial w/\partial t$). In the second part, the more difficult task of defining the spatial variability of the velocity components is tackled, and the resulting data used to determine the relative importance of the nonlinear convective terms ($u\partial u/\partial x + w\partial u/\partial z$ and $u\partial w/\partial x + w\partial w/\partial z$).

5.1. Time Dependence

Figure 4 describes the time history of the water surface elevation, $\eta(t)$, measured at the focal location and compares the measured data, indicated by the solid symbols, with several different wave models. The first, indicated by the thin line, corresponds to a linear wave model based upon the free waves generated at the wave paddle. These waves define the input spectrum represented by the dashed line in Figure 2. It is clear from both Figures 2 and 4 that the neglect of the nonlinear wave–wave interactions and, in particular, the tendency of the local interactions to move energy into the high frequencies, leads to a greater energy density in the vicinity of the extreme event. As a result, both the "steepness" of the wave profile ($\partial\eta/\partial t$ at $t = 0$) and the overall crest–trough asymmetry are significantly larger than that predicted by a linear solution. Indeed, given the very poor description of the water surface profile this linear solution will not be considered further. In contrast, the solid line given in Figure 4 corresponds to the time-stepping procedure outlined in Section 3. This model is in good agreement with the measured data at all times and, given the nature of the initial conditions (see above), adequately reflects the importance of the nonlinear wave–wave interactions.

Figure 4 also compares the measured data with an 18th-order steady wave solution based on the method proposed by Sobey *et al.* (1987). This solution, which is indicated by a dashed line, assumes that the large wave event propagates without change of form and is based upon a representative wave height and wave period. In the present case, the input parameters were chosen to provide the best-possible fit to the steepest section of the wave profile, since it is here that the maximum water particle accelerations arise. As a result, the wave height (H) was based upon the distance between the maximum wave crest (occurring at $t = 0{\cdot}18$ s in Figure 4) and the preceding wave trough ($t = -0{\cdot}25$ s); while the wave period (T) was determined from the down-crossings identified either side of the maximum slope ($t = -0{\cdot}5$ s and $0{\cdot}4$ s). Although this approach differs considerably from the usual method of applying a regular wave solution, subsequent comparisons have shown that it provides the best-possible description of the water particle motion. Indeed, it is common in design practice to base a regular wave solution on a zero up-crossing period and the included wave height, or that occurring between two up-crossings. Preliminary calculations, not presented in this paper, indicate that if such an approach is adopted the results would (in this case) significantly underestimate almost every aspect of the wavefield.

In Figure 5(a), the time history of the horizontal water particle velocity measured at the still water level ($z = 0$) is compared to the various wave models. On the right-hand side of this figure, ($t > 0$) the measured data corresponds to velocities arising beneath the largest wave crest. Comparisons between this data and the steady wave solution suggest that although this model provides a reasonable description of the water surface elevation in the vicinity of the extreme event (Figure 4), it significantly overpredicts the maximum velocities

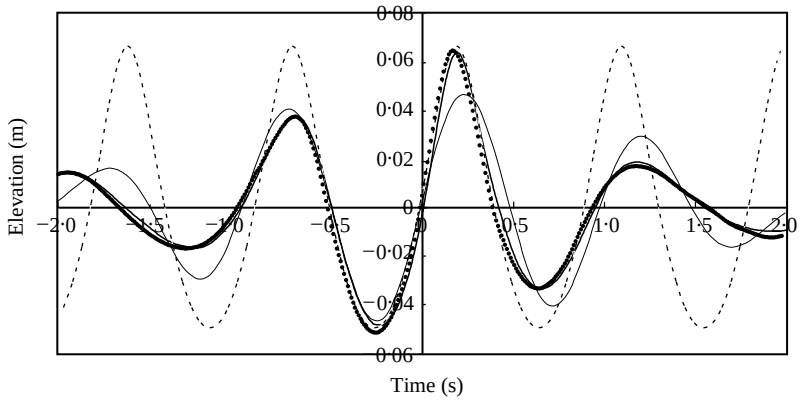

Figure 4. Predicted water surface elevations, $\eta(t)$: ●, measured data; ——, linear theory; ------, steady nonlinear wave theory; ————, time-stepping solution.

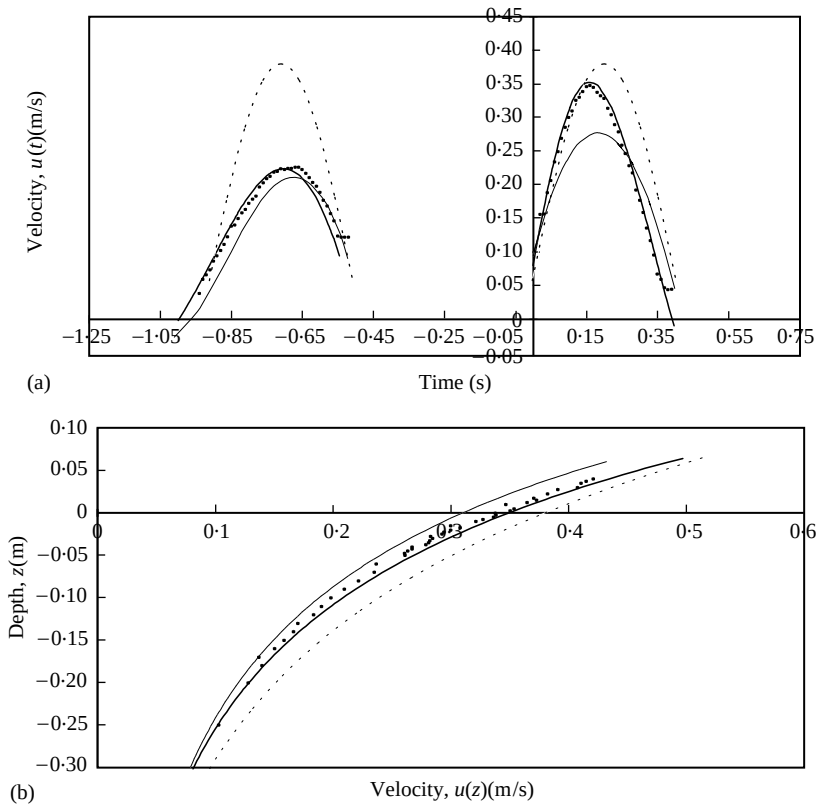

Figure 5. Horizontal velocity. (a) $u(t)$ at $z = 0$ and (b) $u(z)$ at $t = 0{\cdot}18$ s: ●, measured data; ———, linear random wave theory; ------, steady nonlinear wave theory; ————, time-stepping solution.

arising at $t = 0{\cdot}18$ s. In contrast, the thin line presented in Figure 5(a) corresponds to an alternative linear formulation, usually referred to as linear random wave theory, in which the included linear harmonics are based upon a Fourier fit to the measured water surface elevation rather than the free waves generated at the wave paddle. In this case, the predicted

velocities have been "stretched" or empirically corrected using the Wheeler transformation (Wheeler 1970). This approach is necessary to remove the effect of high-frequency contamination (Sobey 1990) arising due to the extrapolation of the solution to the instantaneous water surface. In the present paper, this approach is included not because it is expected to give the best results, but because it represents a commonly applied design solution. However, it is clear from Figure 5(a) that although this solution is based upon a Fourier fit to the measured surface, the empirical correction combined with the misinterpretation of the nonlinear wave components (they are all assumed to be free waves satisfying the linear dispersion equation), leads to a very significant underprediction of the fluid velocities. In contrast, the time-stepping procedure indicated by the solid line is in good agreement with the velocity data. These results are consistent with BST in that they confirm that a good description of the water surface elevation does not provide a sufficient basis for a realistic prediction of the underlying water particle kinematics. Indeed, the neglect of either the unsteadiness or the nonlinearity may be expected to produce significant errors.

On the left-hand side of Figure 5(a) ($t < 0$) the measured data corresponds to the horizontal velocities measured beneath the preceding wave crest. In this case, the time-stepping procedure is again in good agreement with the measured data; while the underprediction of the linear random wave theory is much reduced. This latter agreement arises because the preceding wave is less steep and therefore the nonlinearity less significant. However, it does not follow that a steady wave solution, based on a modified wave height and wave period, would give similarly good results since although the nonlinearity has reduced the dispersive properties (or unsteadiness) remain.

Figure 5(b) concerns the depth variation in the maximum horizontal velocities arising beneath the largest wave crest ($u(z)$ at $t = 0{\cdot}18$ s). The measured data is again compared to a steady wave solution, a linear random wave theory (with empirical correction) and the present time-stepping procedure. These results confirm that while the steady solution overpredicts and the linear random wave theory underpredicts, the time-stepping solution provides a good description of the measured data throughout the water column. As one might expect, the differences between the various models are largest close to the water surface. Indeed, at greater depths beneath the surface, there is increasing agreement between the linear random wave theory and the time-stepping procedure. An explanation for this lies in the fact that in deep water the dominant nonlinear interactions involve a shift of energy into the high frequencies (Figure 2). These components decay rapidly with depth, and consequently the fluid motion within the interior of the flow becomes increasingly linear. However, comparisons between the present results and the numerical calculations undertaken by Smith & Swan (1997) suggest that these arguments only apply in deep water. In intermediate and shallow water the low-frequency, or frequency-difference terms, become significant. These correspond to the global interactions, or set-down beneath the wave group, and thus decay very gradually with depth. As a result, a linear solution tends to overestimate the fluid velocities arising in the lower fluid layers. Although the results presented in Figure 5(a, b) specifically relate to the horizontal water particle velocities, similar trends were also observed when comparing the vertical velocity components with the above noted wave models.

Having measured the time history of the water particle velocities, $u(t)$ and $w(t)$, at a large number of spatial locations, the individual data records were curve fitted and numerically differentiated to define the time history of the unsteady or local water particle accelerations, $\partial u/\partial t(t)$ and $\partial w/\partial t(t)$. Figure 6(a) concerns the horizontal component of the unsteady acceleration "measured" at the still water level ($z = 0$) in the vicinity of the extreme wave event ($x = 0$). Within this figure the laboratory data are again compared to a linear random wave theory with empirical correction, a nonlinear steady wave solution, and the proposed

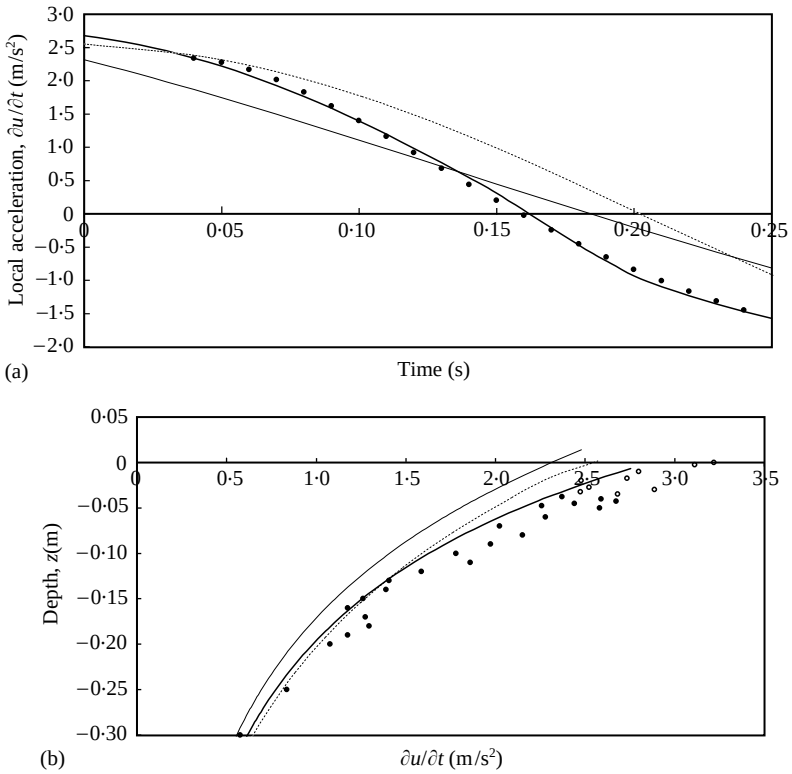

Figure 6. Local maximum acceleration. (a) $\partial u/\partial t(t)$ at $z = 0$ and (b) $\partial u/\partial t(z)$ at $t = 0$: ●, measured data; ○, data involving extrapolation; ———, linear random wave theory; - - - - - -, steady nonlinear wave theory; ————, time-stepping solution.

time-stepping scheme. These comparisons confirm the importance of the nonlinear wave harmonics when seeking to define the maximum local accelerations arising close to the water surface. For example, the linear random wave theory is shown to underestimate the present data by as much as 30%. This result is particularly important since in the vicinity of the focal position ($t = 0$), which corresponds to the zero up-crossing, the magnitude of the "empirical" correction (Wheeler 1970) applied within the linear random wave theory is very small. As a result, the observed difference between the measured data and this theory unambiguously reflects the misinterpretation of the nonlinear wave harmonics. Furthermore, the inability of the nonlinear steady wave model to describe either the maximum local acceleration, or indeed its variation with time, confirms that the unsteadiness of the wave event is important even over relatively short time periods. In contrast, the present timestepping procedure provides a good description of the measured data.

Figure 6(b) concerns the depth variation in the unsteady component of the horizontal acceleration arising directly beneath the focal event ($x = 0$, $t = 0$). These data were again produced by curve fitting and numerically differentiating the time history of the horizontal velocities recorded at $x = 0$. To determine the maximum value of this acceleration above the level of the wave trough (i.e., where the velocity signals become intermittent) some extrapolation of the velocity data within the time domain was necessary, particularly close to $z = 0$. Where this approach has been applied, the respective data points given in Figure 6(b) are identified by open symbols. As a consequence of the curve fitting and numerical differentiation, the data presented in Figure 6(b) is more scattered than the velocity profile

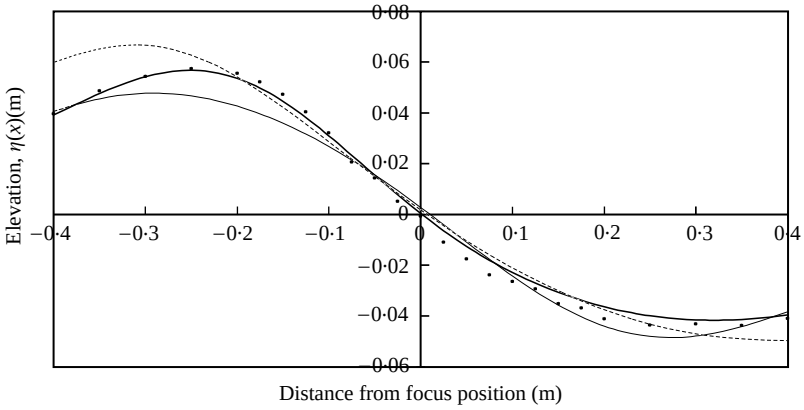

Figure 7. Spatial description of the water surface elevation, $\eta(x)$ at $t = 0$: ●, measured data; ———, linear random wave theory; ------, steady nonlinear wave theory; ————, time-stepping solution.

presented previously [Figure 5(b)]. Nevertheless, the inability of either the linear random wave theory or the steady nonlinear wave theory to describe the data is clear, whereas the time-stepping procedure is in reasonable agreement.

Although the present paper is primarily concerned with the accelerations associated with the extreme wave event, comparisons similar to those presented in Figure 6(a) were also undertaken in the vicinity of the preceding zero up-crossing ($t = -1{\cdot}0$ s in Figure 4). In this case both the time-stepping procedure and the linear random wave theory are in good agreement with the measured data. This is consistent with our previous discussion of the water particle velocities arising beneath less extreme waves, and explains why Zelt *et al.* (1995) found reasonably good agreement between measured and predicted accelerations based on a linear formulation. Indeed, the present results also appear to be consistent with Stansberg & Gudmestad (1996) in which they concluded that detailed measurements of the maximum water particle accelerations arising close to the water surface in highly nonlinear waves were required before the success (or otherwise) of an empirically corrected linear random wave theory could be accurately assessed.

5.2. Spatial Dependence

The previous comparisons have clearly demonstrated the importance of the nonlinear wave–wave interactions. In the present section, we will further demonstrate that, in respect of a spatial representation, additional errors arise because a steady wave theory assumes that the wave-form propagates without change of form, whilst a linear random wave theory assumes that all the wave components are freely propagating and therefore satisfy the linear dispersion equation. In practice, many of the nonlinear harmonics will represent bound waves, travelling at very different phase velocities. One way to demonstrate this effect is to consider a spatial description of the water surface elevation, $\eta(x)$, at the instant of wave focusing ($t = 0$). Figure 7 shows that within this frame of reference, the nonlinear steady wave theory neglects the evolution of the wave field and essentially reproduces the time history of the surface elevation with horizontal scaling (i.e., the wave height remains constant). Such a solution is clearly inadequate, leading to a large over-prediction of both the wave height and the crest elevation recorded in the spatial domain at the instant of wave focusing. (Note: In an unsteady wave field these values differ from the corresponding values recorded in the time domain.) Likewise, a linear random wave theory produces an equally

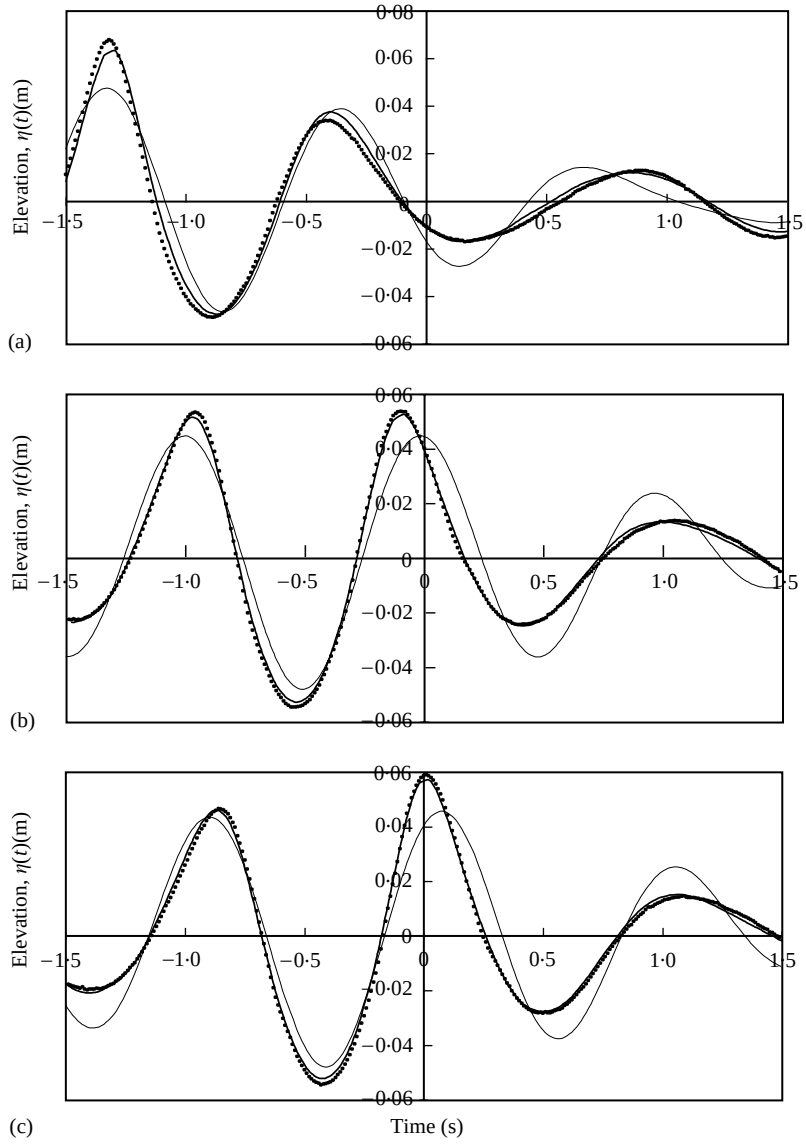

Figure 8. Water surface elevations, $\eta(t)$, (a) $x = -0{\cdot}90$ m, (b) $x = -0{\cdot}40$ m and (c) $x = -0{\cdot}25$ m: ●, measured data; ———, linear random wave theory; ————, time-stepping solution.

poor description of the measured data. In particular, it underestimates the advancing crest height (i.e., $\eta(x)$ at $x = -0{\cdot}25$ m) by some 25%. Accordingly, one would expect this latter solution to underestimate the spatial gradient of the surface profile at focus.

To further examine the spatial variability of the water surface elevation, Figure 8(a–c) provides time histories of the water surface elevation recorded at three upstream locations ($x = -0{\cdot}90$, $-0{\cdot}40$ and $-0{\cdot}25$ m). In each case, the measured data is compared to both a linear random wave theory and the present time-stepping procedure. These comparisons again confirm the inability of a linear random wave theory to model the spatial evolution of an extreme wave-form. In contrast, the time-stepping procedure is in good agreement with the measured data at all points in space and time.

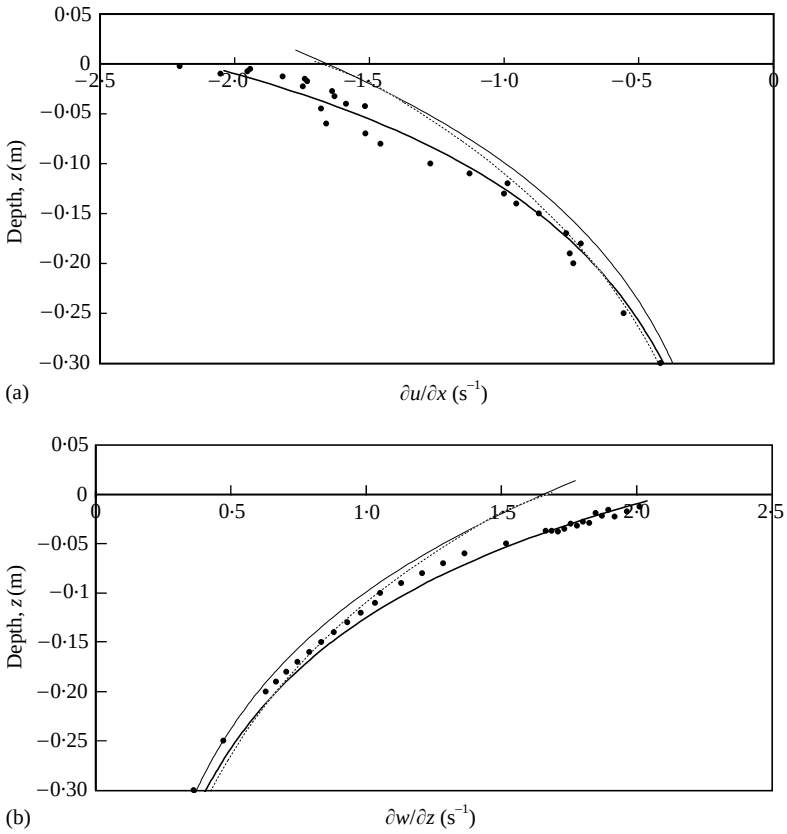

Figure 9. Spatial gradients. (a) $\partial u/\partial x(z)$ at $x = 0$, $t = 0$ and (b) $\partial w/\partial z(z)$ at $x = 0$, $t = 0$. ●, measured data; ———, linear random wave theory; - - - - -, steady nonlinear wave theory; ————, time-stepping solution.

Figure 9(a) and 9(b) provides two examples of the depth variation in the spatial gradients of the velocity components ($\partial u/\partial x$ and $\partial w/\partial z$). This data was defined by numerically differentiating velocity profiles corresponding to $u(x)$ and $w(z)$ recorded at the instant of wave focusing. In the former case, it should be noted that the spatial description of the velocity components in the horizontal direction are not as well defined as those in the vertical direction (i.e., a 24 point fit rather than a 50 point fit). As a result, the spatial gradients presented in Figure 9(a) show more scatter than those presented in Figure 9(b). Nevertheless, it is clear from both of these figures that neither the linear random wave theory nor the nonlinear steady wave theory provides an adequate description of the spatial gradients appropriate to the calculation of the convective accelerations. In contrast, the time-stepping procedure is in good agreement with the measured data.

6. INERTIAL LOADING

To assess the significance of the present results to inertial loading and, in particular, to determine the relative importance of the various nonlinear contributions, the forces acting on a vertical cylinder extending from the bottom boundary up through the water surface have been calculated. The cylinder is assumed to be rigid with an external diameter of $D = 0{\cdot}1$ m. In relation to the extreme wave event identified in Figure 4, the cylinder has a diameter to wavelength ratio of $D/\lambda = 0{\cdot}1$, and a corresponding Keulegan–Carpenter

number of $UT/D = 3{\cdot}0$. Using these criteria the test conditions are outside the typical diffraction regime ($D/\lambda > 0{\cdot}2$), and it may be assumed that the fluid loading is inertia dominated. This case was specifically chosen such that the nonlinear potential loading originally considered by Rainey (1989, 1995*a*, *b*), and further developed by Faltinsen *et al.* (1995) is directly applicable. Using similar notation to that adopted by Jefferys & Rainey (1994), the potential loads applied to a fixed cylinder are given by:

(i) the Morison's inertia force,

$$F_{IN} = 2\rho \frac{\pi D^2}{4}\left(\frac{\partial u}{\partial t} + u\frac{\partial u}{\partial x} + w\frac{\partial u}{\partial z}\right); \tag{7}$$

(ii) an axial divergence force,

$$F_{AD} = M_x u \frac{\partial w}{\partial z}; \tag{8}$$

(iii) a free surface intersection force,

$$F_{SI} = -\frac{1}{2}\frac{\partial \eta}{\partial x} M_x u^2; \tag{9}$$

where (u, w) are the components of the water particle velocity, ρ is the density and M_x is the added mass per unit length. In this form, equations (7) and (8) describe the distributed forces, having units of N/m, while equation (9) represents a point load acting at the water surface. Rainey (1989) derived these terms using arguments based upon the conservation of energy coupled with the assumption that the position of the water surface is unaffected by the presence of the structure (i.e., it corresponds to the limiting case in which the cylinder is reduced to a line with hydrodynamic properties). In a subsequent paper, Manners & Rainey (1992) derived identical results using an independent method based on pressure integration. The advantage of this latter approach is that it provides some physical insight into the source of the axial divergence force, suggesting that it is related to the rate of change of added mass. The mathematical origin of this additional force is also clearly explained. More recently, Faltinsen *et al.* (1995) considered the wave forces acting on a vertical cylinder in which the flow regime, involving a cylinder of diameter D and regular waves of amplitude A and wavenumber k, is characterised by $kA \ll 1$, $kD \ll 1$, but $A/D = \mathcal{O}(1)$. This solution differs from the previous work by Rainey (1989) and Manners & Rainey (1992), in that it includes the distortion of the incident waves due to the presence of the body. In comparing their results with Rainey (1989), Faltinsen *et al.* (1995) noted that the axial divergence term appears unchanged, but that the "third-order" free surface force [equation (9)] is substantially increased. This point is further investigated by Rainey (1995*a*) in which he demonstrated, again using energy conservation, that the distortion of the free surface produces an additional force which is quite distinct from the mechanisms identified by Rainey (1989). This so-called surface distortion force represents an additional point load acting at the water surface:

$$F_{SD} = \frac{7}{2g}\frac{\partial u}{\partial t} M_x u^2. \tag{10}$$

If this force is combined with the surface intersection force, equation (9), the total load is identical to that predicted by Faltinsen *et al.* (1995). Following this work, Malenica & Molin (1995) have provided further insight into the characteristics of third-harmonic diffraction, and Newman (1996) has extended the method proposed by Faltinsen *et al.*

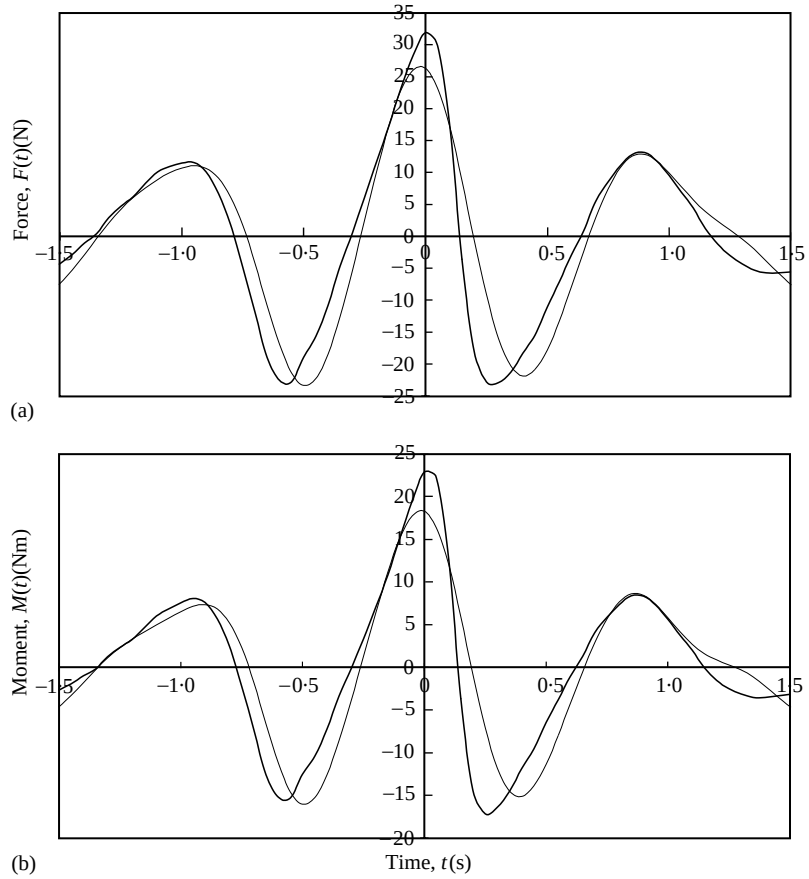

Figure 10. (a) Total horizontal force, $F(t)$ and (b) total over-turning moment, $M(t)$: ———, linear random wave theory; ————, time-stepping solution.

(1995) to model (uni-directional) irregular waves. In this latter example, Newman assumed that up to a third order of approximation, a deep-water incident-wave system could be represented by linear superposition of the first-order potentials with an appropriate modification of the dispersion equation. Unfortunately, the data presented in Section 4 (particularly Figures 2, 4 and 6) suggest that in the case of a highly nonlinear wave group, typically associated with "ringing" events, this approach provides a poor description of both the water surface elevation and the underlying water particle accelerations.

In the present example, we will set aside the rigorous ordering of the force components adopted by previous researchers, and merely apply our best estimate of the underlying water particle kinematics. Although this approach will clearly introduce errors due to the absence of some higher-order force components (the solutions for which do not exist), it will provide guidance as to the relative importance of the above noted force components and, in particular, will define the dominant source of the nonlinearity. For example, the unsteady inertia force identified by the first term in equation (7) is often referred to as a "first-order" force. However, this description solely arises as a result of the applied wave theory. If a nonlinear wave theory is adopted to model the associated wave kinematics, real nonlinear force components result. In Figure 10(a) and 10(b) the force components given in equations (7)–(10) have been summed to give a time history of the total base shear and the corresponding over-turning moment produced by the wave-form discussed in Section 5. In each of

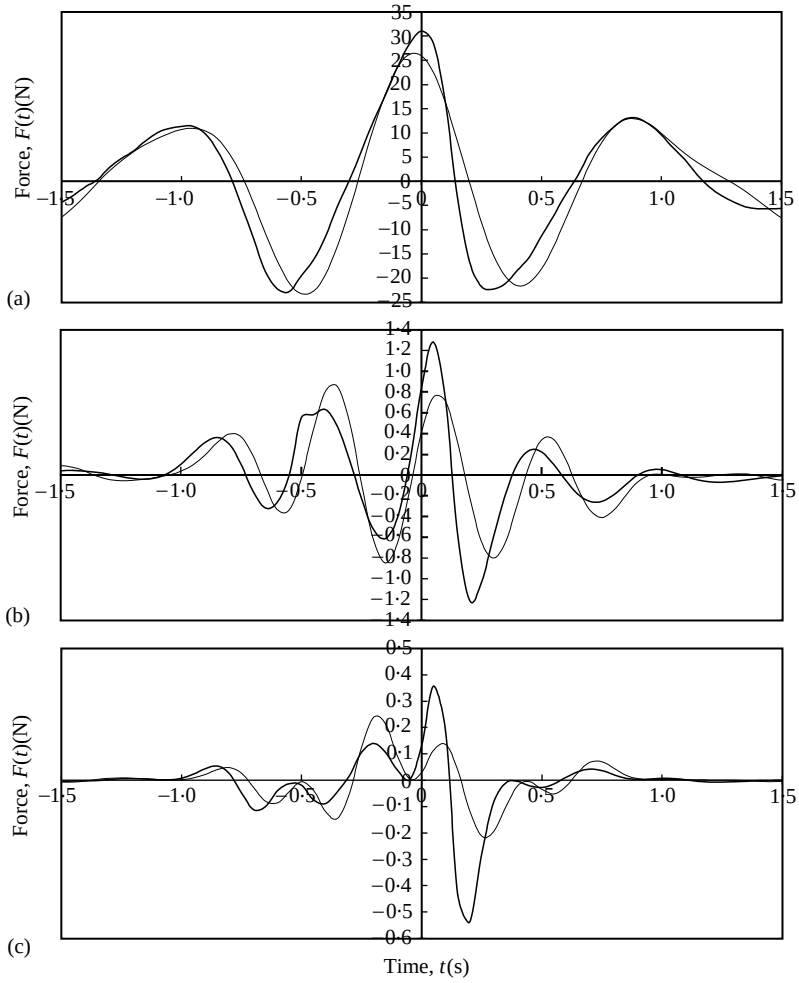

Figure 11. Horizontal force components. (a) Morison's inertia force, (b) axial divergence, and (c) free surface forces: ———, linear random wave theory; ————, time-stepping solution.

these figures the time-base is identical to that used to define the wave profile in Figure 4, and the calculations have been undertaken using two different wave models. The first is based upon an empirically corrected linear random wave theory, and therefore represents a typical design solution, while the second is based upon the present time-stepping procedure. In Figure 10(a), the maximum total base shear predicted according to the linear wave model is approximately 20% smaller than that predicted by the nonlinear solution. Likewise, the total over-turning moment [Figure 10(b)] is underestimated by almost 30%. These results merely reflect the inability of a linear random wave theory (or, indeed, any other linear model) to accurately predict the maximum water particle accelerations arising close to the water surface.

The three components of the horizontal force are further considered in Figure 11(a–c), and their relative contribution to the total base shear assessed. Figure 11(a) concerns the Morison's inertia force [equation (7)] based upon the total water particle acceleration, Figure 11(b) the axial divergence force [equation (8)], and Figure 11(c) the total point force acting at the free surface [equations (9) and (10)]. Comparisons between Figure 11(b) and

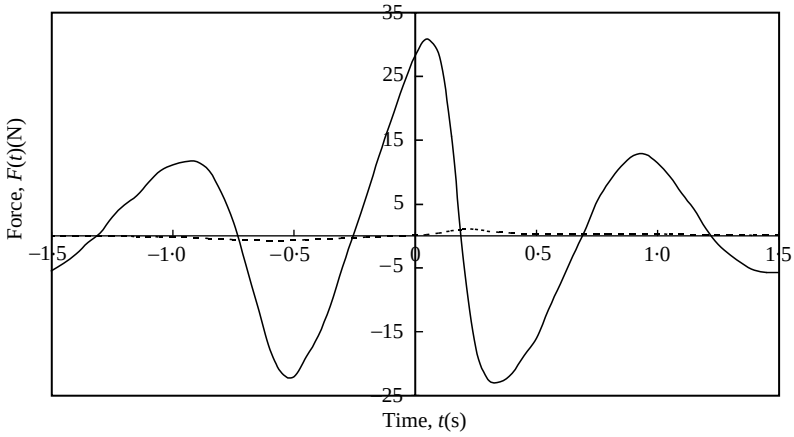

Figure 12. Contributions to Morison's inertia force: ————, unsteady acceleration; ------, convective acceleration.

11(c) suggest that the axial divergence term is more significant than the free surface force and that in both cases, the nonlinear calculations are considerably larger than that predicted by a linear solution. However, the relative magnitude of these terms is small in comparison with the maximum value of the Morison's inertia term [Figure 11(a)]. Indeed, the results presented in Figure 11(a–c) suggest that provided the total water particle acceleration is correctly modelled using an appropriate nonlinear wave theory, Morison's inertia force integrated up to the instantaneous water surface provides a reasonable approximation to the total potential load.

This point is further considered in Figure 12 where the unsteady and convective contributions to Morison's inertia force are calculated using the present time-stepping procedure. These results confirm that the convective component is very small and since it is also approximately 90° out of phase with the unsteady component, the nonlinear convective accelerations make no significant contribution to the maximum value of either the total base shear or the over-turning moment. The maximum value of the inertia loading is therefore primarily dependent upon the unsteady water particle accelerations, particularly the large nonlinear contributions arising close to the water surface.

Although the maximum nonlinear inertia loading is undoubtedly important, it was noted in Section 2.0 that the principal practical concerns relate to the onset of dynamic response. As a result, the frequency content of the applied forcing is of considerable interest. Figure 13 describes two force spectra produced by taking a fast Fourier transform of the time history of the total base-shear predicted using the above noted wave models. This figure clearly suggests that if the fluid motions are predicted by an appropriate nonlinear wave model (i.e., the present time-stepping solution), large fluid loads accounting for approximately 10% of the maximum arise at high frequencies within the range 2–3 times the peak spectral frequency. In contrast, the force spectra based upon a linear random wave theory predicts significantly lower forces within this range (approximately 1% of the maximum). Furthermore, Figure 14 provides four separate force spectra corresponding to the unsteady inertia force, the convective inertia force, the axial divergence force, and the total free surface force. In each case, these calculations are again based upon the respective contributions to the total base shear assessed using the time-stepping solution. These results confirm that the contribution arising from the unsteady inertia force is dominant. In particular, this term is associated with high-frequency force components that are at least one order of magnitude

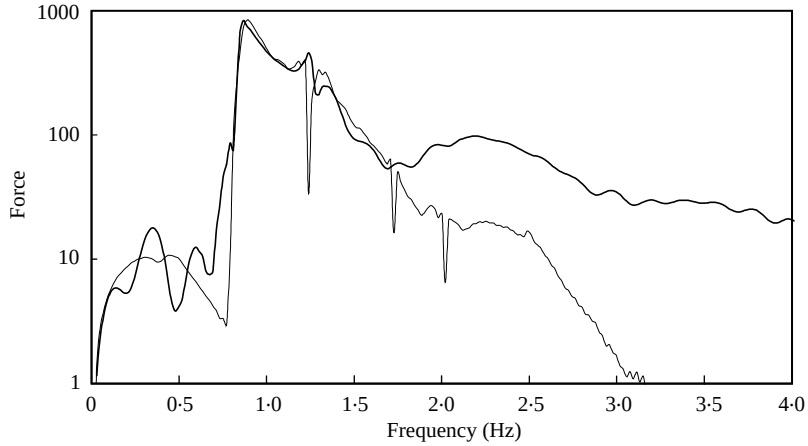

Figure 13. Frequency spectra of total horizontal force: ———, linear random wave theory; ————, time-stepping solution.

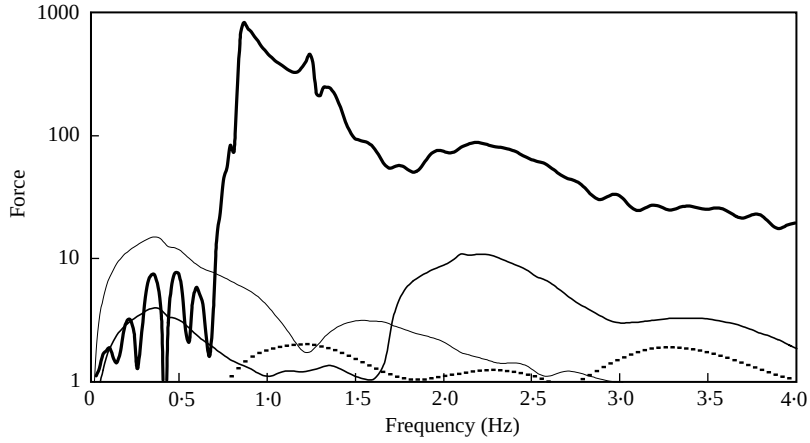

Figure 14. Frequency spectra of horizontal force components: ▬▬, unsteady Morison's inertia force; ——, convective Morison's inertia force; ————, axial divergence force; - - - - -, free surface forces.

larger than those associated with the axial divergence term. For example, if one considers the force components within the above noted range (i.e., 2–3 times the peak spectral frequency), the contribution due to the nonlinear unsteady components is again of the order of 10% of the maximum. In contrast, the contribution due to axial divergence term is of the order of 1%, while the convective and free surface terms contribute less than 0·2%.

7. CONCLUDING REMARKS

The present paper has considered the water particle accelerations arising beneath a highly nonlinear transient wave group. A new series of laboratory observations have been presented in which the time history of the water particle velocities have been recorded at a large number of spatial locations. This data is used to define the unsteady and convective components of the water particle acceleration. Comparisons with these results suggest that although a linear random wave theory (based on a Fourier transform of the measured water

surface elevation) and a steady nonlinear wave theory (based on an "equivalent" wave height and wave period) can provide a reasonable description of the water surface profile in the vicinity of the extreme event, this is not sufficient to ensure a good description of the underlying flow field. Indeed, neither of these wave models is able to predict the large unsteady accelerations arising close to the water surface. Furthermore, although the linear random wave theory partially incorporates the unsteadiness of the wave motion, it is unable to model the spatial evolution of a large transient wave. As a result, neither this solution nor a steady wave model provides a good description of the spatial gradients of the velocity field used to define the convective accelerations.

These discrepancies arise due to the neglect, or misinterpretation, of the nonlinear wave–wave interactions. In particular, spectral analysis of the water surface elevation measured at the focal location suggests that the local interactions produce a significant shift of energy into the high-frequency components. This produces an increase in the local energy density resulting in steeper waves with larger water particle accelerations. In contrast to the above noted wave models, a fully nonlinear unsteady wave solution based upon the time-stepping procedure originally proposed by Fenton & Rienecker (1980), appears to be in good agreement with the measured data. In particular this solution, which is simply based upon initial conditions derived from the underlying linear wave spectrum, provides an accurate representation of the energy shifts within the vicinity of the focused event. As a result, a good description of the underlying water particle accelerations is achieved. Although there are undoubtedly other time-stepping procedures that would be equally successful, it may be concluded from the present results that an accurate prediction of the nonlinear accelerations can only be determined by a wave model that fully incorporates both the unsteadiness and the nonlinearity of an extreme wave event.

Finally, to emphasise the importance of these results, the inertia forces acting on a vertical surface-piercing cylinder were determined, and the relative importance of the nonlinear contributions assessed. These results apply to a structure outside the typical diffraction regime (i.e., $D/\lambda < 0{\cdot}2$) and suggest that provided the unsteady water particle accelerations are described by an appropriate nonlinear wave model, the standard Morison's inertia term integrated up to the instantaneous water surface provides a good description of the maximum loads. Furthermore, spectral analysis of the predicted forces suggests that the dominant source of the high-frequency forcing, believed to be responsible for the onset of structural "ringing", arises due to the nonlinearity of the wave motion rather than the additional forces identified in equations (7)–(10).

The extent to which such arguments are generally valid clearly requires further detailed investigation, involving the generation of realistic ocean spectra and, ideally, comparisons with measured rather than predicted force data. It is intended that such comparisons will be provided in a second, Part II, paper. However, the present results clearly suggest that important nonlinear forcing may arise as a consequence of the nonlinearity of the wave motion and that such forces can only be predicted via the application of a fully nonlinear and unsteady wave model. These findings appear to be in partial agreement with the discussion provided by Rainey (1995*a*) in which he commented that the additional surface distortion force is perhaps more relevant to the prediction of third-harmonic forces associated with small waves, than in exciting "ringing". The present paper merely takes this argument one step further and suggests that since the onset of structural "ringing" is known to be associated with the steepest waves within a sea state, the potential loading must be based upon a fully nonlinear description of the water particle acceleration. When this is achieved, both the axial divergence force and the local free surface forces, derived from a limited perturbation expansion, become less relevant to the prediction of either the maximum potential loads or the high-frequency forcing.

References

Baldock, T. E. & Swan, C. 1994 Numerical calculations of large transient water waves. *Applied Ocean Research* **16,** 101–112.

Baldock, T. E., Swan, C. & Taylor, P. H. 1996 A laboratory study of nonlinear surface waves on water. *Philosophical Transactions of the Royal Society*, Series A **354,** 649–676.

Craig, W. & Sulem, C. 1993 Numerical simulation of gravity waves. *Journal of Computational Physics* **108,** 73–83.

Dean, R. G. 1965 Stream function representation of non-linear ocean waves. *Journal of Geophysical Research* **70,** 4561–4572.

Dold, J. W. & Peregrine, D. H. 1984 Steep unsteady waves: an efficient computational scheme. *Proceedings of the* 19*th International Conference on Coastal Engineering*, Vol. 1, pp. 955–967, Houston, U.S.A., ASCE.

Faltinsen, O. M., Newman, J. N. & Vinje, T. 1995 Nonlinear wave loads on a slender vertical cylinder. *Journal of Fluid Mechanics* **289,** 179–198.

Fenton, J. D. 1985 A fifth order Stokes' theory for steady waves. *ASCE Journal of Waterways, Port, Coastal and Ocean Engineering* **111,** 216–234.

Fenton, J. D. & Rienecker, M. M. 1980 Accurate numerical solutions for nonlinear waves. *Proceedings of the* 17*th International Conference on Coastal Engineering*, Vol. 1, pp. 50–69, Sidney, Australia, ASCE.

Gear, C. W. 1971 *Numerical Initial Value Problems in Ordinary Differential Equations*, 191–197. Englewood Cliffs, NJ: Prentice Hall.

Jefferys, E. R. & Rainey, R. C. T. 1994 Slender body models of TLP and GBS "ringing". *Proceedings of the* 7*th International Conference on the Behaviour of Offshore Structures* (BOSS), Vol. 2, pp. 587–605, Boston, U.S.A.

Johannessen, T. B. & Swan, C. 1997 Numerical calculations of 2-D transient waves. Part I: comparisons with laboratory data. *Applied Ocean Research* **19,** 293–308.

Johannessen, T. B. & Swan, C. 2001 A laboratory study of the focusing of transient and directionally spread surface water waves. *Proceedings of the Royal Society*, Series A, **457,** 971–1006.

Jonathan, P. & Taylor, P. H. 1995 Irregular, non-linear waves in a spread sea. *Proceedings of the* 14*th International Conference on Offshore Mechanics and Arctic Engineering* (OMAE), Vol. 1A, pp. 9–16, Copenhagen, Denmark.

Lighthill, M. J. 1979 Waves and hydrodynamic loading. *Proceedings of the* 2*nd International Conference on the Behaviour of Offshore Structures* (BOSS), Vol. 1, pp. 1–40, Cranfield, U.K.

Longuet-Higgins, M. S. 1974 Breaking waves in deep and shallow water. *Proceedings of the* 10*th International Conference on Navel Hydrodynamics*, pp. 597–605, Cambridge, MA, U.S.A.

Longuet-Higgins, M. S. 1987 The propagation of short surface waves on longer gravity waves. *Journal of Fluid Mechanics* **177,** 293–306.

Longuet-Higgins, M. S. & Stewart, R. W. 1960 Changes in the form of short gravity waves on long waves and tidal currents. *Journal of Fluid Mechanics* **8,** 565–583.

Longuet-Higgins, M. S. & Cokelet, E. D. 1976 The deformation of steep surface waves on water. A numerical method of computation. *Proceedings of the Royal Society*, Series A **350,** 1–26.

Manners, W. & Rainey, R. C. T. 1992 Hydrodynamic forces on fixed submerged cylinders. *Proceedings of the Royal Society*, Series *A* **436,** 13–32.

Malenica, S. & Molin, B. 1995 Third-harmonic wave diffraction by a vertical cylinder. *Journal of Fluid Mechanics* **303,** 203–229.

Newman, J. N. 1996 Nonlinear scattering of long waves by a vertical cylinder. In *Waves and Nonlinear Processes in Hydrodynamics* (eds J. Grue *et al.*). Dordrecht: Kluwer Academic Publishers.

Rainey, R. C. T. 1989 A new equation for calculating wave loads on offshore structures. *Journal of Fluid Mechanics* **204,** 295–324.

Rainey, R. C. T. 1995*a* The hydrodynamic load at the intersection of a cylinder with the water surface. *Proceedings of* 10*th International Workshop on Water Waves & Floating Bodies* (ed. R. Eatock Taylor), pp. 207–210, Oxford, U.K.

Rainey, R. C. T. 1995*b* Slender-body expressions for the wave load on offshore structures. *Proceedings of the Royal Society*, Series A **450,** 391–416.

Rapp, R. J. & Melville, W. K. 1990 Laboratory measurements of deep-water breaking waves. *Philosophical Transactions of the Royal Society*, Series A **331,** 735–800.

Sharma, J. N. & Dean, R. G. 1981 Second-order directional seas and associated wave forces. *Journal of the Society of Petroleum Engineers* **4,** 129–140.

Skyner, D. 1996 A comparison of numerical predictions and experimental measurements of the internal kinematics of a deep-water plunging wave. *Journal of Fluid Mechanics* **315,** 51–64.

Smith, S., & Swan, C. 1997 Kinematic predictions in large shallow water waves. *Proceedings of* 25*th International Conference on Coastal Engineering*, U.S.A., Vol. 1, pp. 502–515, Orlando, FL, ASCE.

Sobey, R. J., Goodwin, P., Thieke, R. J. & Westberg, R. J. 1987 Applications of Stokes, Cnoidal and Fourier wave theories. *ASCE Journal of Waterways*, *Port*, *Coastal and Ocean Engineering* **113,** 565–587.

Sobey, R. J. 1990 Wave theory predictions of crest kinematics. In Water *Wave Kinematics* (eds A. Torum & O. T. Gudmestad), Vol. 1, pp. 215–231. Dordrecht: Kluwer Academic Publishers.

Sobey, R. J. 1992 A local Fourier approximation method for irregular wave kinematics. *Applied Ocean Research* **14,** 93–105.

Stansberg, C. T. 1993 Second-order numerical reconstruction of laboratory generated random waves. *Proceedings of* 12*th International Conference on Offshore Mechanics and Artic Engineering* (OMAE), Vol. 2, pp. 143–151, Glasglow, Scotland.

Stansberg, C. T. 1997 Comparing "ringing" loads from experiments with cylinders with different diameters — an experimental study. *Proceedings of* 8*th International Conference on the Behaviour of Offshore Structures* (BOSS), pp. 95–109, Delft, The Netherlands.

Stansberg, C. T. & Gudmestad, O. T. 1996 Nonlinear random wave kinematics models verified against measurements in steep waves. *Proceedings of the* 15*th International Conference on Offshore Mechanics and Artic Engineering*, Vol. 1A, pp. 15–24, Florence, Italy.

Wheeler, J. D. 1970 Method of calculating forces produced by irregular waves. *Proceedings of the Offshore Technology Conference* (OTC), Vol. 1, pp. 71–82, Houston, U.S.A.

Ye, M. & Zhang, J. 1994 Predictions of unidirectional irregular wave kinematics and evolution. *Proceedings of the Offshore Technology Conference* (OTC), Vol. 1, pp. 43–54, Houston, U.S.A.

Zakharov, V. E. 1968 Stability of periodic waves of finite amplitude on the surface of a deep fluid. *Journal of Applied Mechanics & Technical Physics* (English Transl.) **9,** 86–94.

Zelt, J. A., Gudmestad, O. T. & Skjelbreia, J. E. 1995 Fluid accelerations under irregular waves. *Appied Ocean Research* **17,** 43–54.

Zhang, J., Yang, J. & Wen, J. 1998 Hybrid wave models and their application. *Proceedings of the International Symposium on Ocean Wave Kinematics*, *Dynamics and Loads on Structures* (ASCE). (ed. J. Zhang), Vol. 1, pp. 25–33, Houston, TX, U.S.A.